Geometry-induced wave-function collapse

Li-Li Ye,[1,2] Chen-Di Han,[2] Liang Huang,[1,*] and Ying-Cheng Lai[2,3,†]

[1]Lanzhou Center for Theoretical Physics, Key Laboratory of Theoretical Physics of Gansu Province, and Key Laboratory for Magnetism and Magnetic Materials of MOE, Lanzhou University, Lanzhou, Gansu 730000, China

[2]School of Electrical, Computer and Energy Engineering, Arizona State University, Tempe, Arizona 85287, USA

[3]Department of Physics, Arizona State University, Tempe, Arizona 85287, USA

(Received 4 February 2022; revised 9 June 2022; accepted 19 July 2022; published 12 August 2022)

When a quantum particle moves in a curved space, a geometric potential can arise. In spite of a long history of extensive theoretical studies, to experimentally observe the geometric potential remains a challenge. What are the physically observable consequences of such a geometric potential? Solving the Schrödinger equation on a truncated conic surface, we uncover a class of quantum scattering states that bear a strong resemblance to the quasiresonant states associated with atomic collapse about a Coulomb impurity, a remarkable quantum phenomenon in which an infinite number of quasiresonant states emerge. A characteristic defining feature of such collapse states is the infinite oscillations of the local density of states (LDOS) about the zero energy point separating the scattering from the bound states. The emergence of such states in the curved (Riemannian) space requires neither a relativistic quantum mechanism nor any Coulomb impurity: they have zero angular momentum and their origin is purely geometrical, hence the term "geometry-induced wave-function collapse." We establish the collapsing nature of these states through a detailed comparative analysis of the behavior of the LDOS for both the zero and finite angular momentum states as well as the corresponding classical picture. Potential experimental schemes to realize the geometry-induced collapse states are articulated. Not only does our paper uncover an intrinsic connection between the geometric potential and atomic collapse, it also provides a method to experimentally observe and characterize geometric potentials arising from different subfields of physics. For example, in nanoscience and nanotechnology, curved geometry has become increasingly common. Our finding suggests that wave-function collapse should be an important factor of consideration in designing and developing nanodevices.

DOI: 10.1103/PhysRevA.106.022207

I. INTRODUCTION

When a quantum particle moves on a curved surface, a geometric potential can arise [1,2], which is fundamental to quantum mechanics in the Riemannian geometry. However, it remains a challenge to experimentally observe the geometric potential [3–5]. The main message of this paper is that the conic geometric potential can induce wave-function collapse as manifested by the peculiar behavior of the local density of states (LDOS) typically seen in atomic collapse. Semiclassically, this geometry-induced collapse phenomenon is manifested as a particle's spiraling inward towards a region of large curvature in the classical-quantum correspondence [6,7]. Thus, theoretically, our paper unveils a natural connection between the quantum mechanics in the curved space and the phenomenon of atomic collapse. Experimentally, our finding provides a viable way to meet the challenge of experimentally observing the geometric potential by putting forward measurable quantities as in the recent experimental study of atomic collapse.

The radial component of the Schrödinger equation for a particle on a conic surface [8] can be simplified as the Bessel equation with the $1/r^2$ effective potential. Historically, the study of the $1/r^2$ potential in three dimensions has a long history [6,9–13], which can be induced by diverse physical mechanisms such as particle-charge interactions [11,14] and Efimov physics [15,16]. For example, in the early work by Shortley [6] in 1932, the wave function was set to be zero at the origin. In the work of Case [13] in 1950, a fixed phase was required for the wave functions at the origin. Bound and scattering states under the hard-core boundary condition and zero net outflow from the scattering region were analyzed earlier by Nicholson [9] in 1962 and more recently by Coon and Holstein [11] in 2002. That the three-dimensional (3D) central $1/r^2$ potential can induce a fall to the center associated with both bound and scattering states was analyzed [10,17,18]. There were also works on the 3D central $1/r^2$ potential from different perspectives, such as anomalous symmetry breaking [11] and limit cycles [12].

A recent development in quantum physics is the experimental observation of atomic collapse [19], a phenomenon that was predicted nearly 80 years ago [20–22] to occur in an atom with a superheavy nucleus. In the present paper, we consider particle motion on a curved surface that gives rise to a $1/r^2$ potential in two dimensions [2,8,23–27]. The main

*huangl@lzu.edu.cn
†Ying-Cheng.Lai@asu.edu

contribution of our paper is the establishment of the connection between the quantum behaviors on a curved surface and those associated with atomic collapse, providing a feasible way to experimentally observe the geometric potential. To place our paper in a proper context and to better explain our finding, here we provide a brief description of the phenomenon of atomic collapse.

Consider a hydrogenlike atom of nuclear charge Z with the Coulomb potential $-Z/r$. For $Z > 1/\alpha_0$, where $\alpha_0 \equiv e^2/(\hbar c) \approx 1/137$ is the vacuum fine-structure constant, the eigenenergy becomes complex, signifying the emergence of a resonant state with a finite lifetime for the electron that is inversely proportional to the imaginary part of the eigenenergy. The physical picture is that, in a sufficiently strong Coulomb field, the eigenenergy dives into the hole continuum, and the laws of relativistic quantum mechanics stipulate the creation of an electron-positron pair. Once this happens, the positron is free but the electron and the nucleus will form a quasibound resonant state, as if the electron had collapsed onto the nucleus. From a classical point of view, the electron behaves as if it spiraled inward toward the nucleus. Because of the finite lifetime of the resonant state, the electron will eventually escape the nucleus and couple to the positron [28]. The wave function thus contains two components: one around the Coulomb singularity and another extending to infinity.

From a mathematical point of view, the Dirac equation breaks down in the vicinity of the $1/r$ singularity of the Coulomb potential and some regularized form of the potential should then be used so that the Dirac equation remains valid. Even then, for sufficiently large values of Z, the eigenenergies will still be complex. A general estimate of the required Z values for atomic collapse to occur [18,20] is $Z > 170$, which exceeds the largest known atomic number of any natural element with the fine-structure constant α_0. To experimentally realize atomic collapse, some kind of relativistic quantum materials with a much larger effective fine-structure constant (or a much reduced "speed of light") can be exploited. In graphene, the Fermi velocity of the relativistic quantum quasiparticles is about two orders of magnitude smaller than the vacuum speed of light, so the effective fine-structure constant is on the order of unity, making possible experimental observation of atomic collapse [7,29]. This perspective stimulated theoretical studies of the various aspects of the energy states of an atomic impurity embedded in graphene such as screening [30,31], density of states [7,29,32,33], scattering phase [7,34], and generalization taking into account electron-electron interactions [35]. In 2012, the first experimental observation of atomic collapse in graphene was achieved [19,36], generating subsequent interest in this phenomenon [37–39]. Quite recently, atomic collapse has been predicted to occur in pseudospin-1 Dirac materials with a flat band [40].

The general feature of atomic collapse, i.e., the emergence of infinitely many resonant states [7], can be understood by considering Dirac fermions with energy $\varepsilon < 0$ in the two-dimensional (2D) Coulomb potential $V(r) = -Ze^2/r$. The kinetic energy $K = \varepsilon - V(r)$ is positive for $r < r_* \equiv Ze^2/|\varepsilon|$ and negative for $r > r_*$. If the Dirac particle wavelength $\lambda = \hbar v_F/|\varepsilon|$ (v_F being the Fermi velocity) is smaller than r_*, which occurs if $Z > \hbar v_F/e^2$, then the particle can be trapped inside r_* but only for a finite amount of time before escaping due to the Klein-tunneling mechanism [41]. Since the ratio r_*/λ is independent of the energy, an infinite number of such quasibound states are possible [7]. If one plots the LDOS versus the energy near the zero energy point, infinite oscillations can occur, which is the defining characteristic of atomic collapse.

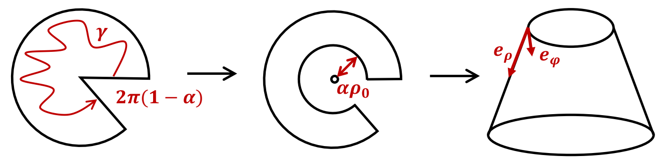

FIG. 1. A truncated conic surface with angular deficit $2\pi(1-\alpha)$ for $0 < \alpha < 1$. The truncation is physically infinitesimal in the sense that the truncated distance away from the apex of the cone ρ_0 is chosen to have the size of only one or two atoms: $\rho_0 \approx 2$ Å.

In this paper, we study particles confined on a curved space and uncover a class of quantum states similar to those that occur in atomic collapse. In general, the characteristics of quantum states on a curved surface constitute a fundamental problem in physics [5]. To derive the Schrödinger equation governing the motion of a particle on a curved surface, an earlier approach was due to DeWitt [42], which was based on the quantization of the classical 2D Lagrangian. A difficulty with this method was that the particles are treated as intrinsically moving in the 2D space, thereby generating the dilemma of "operator ordering ambiguity" that, for a classical function, multiple representative quantum operators may exist. The approach articulated by Jensen, Koppe, and da Costa (JKC) [1,2] overcomes this difficulty, where the Schrödinger equation was derived starting from the 3D Euclidean position space followed by a reduction to a 2D curved surface through an infinitesimally narrow confining potential locally normal to the surface. As a result, a general feature of the Schrödinger equation on a curved surface is a potential term due to the intrinsic curvature of the 2D surface, and thus the so-called geometric potential. This approach has an experimental basis as the effects of the geometric potential on the quantum states have been observed experimentally in electronic systems [3,5] and photonic topological crystals [4]. In fact, the JKC approach has become the standard tool to study quantum mechanics on curved surfaces [43–47].

To be concrete, we study a conic surface with its apex physically infinitesimally truncated in the sense that a circular region about the apex with size of only 1 or 2 Å is removed, as shown in Fig. 1. We employ the JKC method to derive the radial Schrödinger equation on the truncated conic surface [8] and identify an effective potential that has an inverse squared dependence on the distance from the apex of the cone. This potential has a geometric origin, which can be attractive or repulsive depending on the angular momentum quantum number. The analytical solutions of the Schrödinger equation contain both bound and scattering states. Surprisingly, we uncover a class of abnormal scattering states that characteristically resemble the states underlying atomic collapse in a 2D system, e.g., in graphene. Since these unusual states are purely due to the curved geometry without the presence of any heavy nucleus, they are geometry induced. Quantitatively, the "collapse" nature of these states is established through the behavior of the LDOS, which we find exhibits infinite oscillations—the defining characteristic of atomic collapse. Strictly speaking, they are only "collapselike" states because atomic collapse is a relativistic quantum phenomenon but these states have a purely nonrelativistic quantum origin. At the minimal risk of confusion, we still use the term "collapse" for convenience. To draw a stronger analogy of these states with those in atomic collapse, we develop a qualitative analysis of the classical trajectories corresponding to the geometry-induced collapse states. Furthermore, we articulate possible experimental schemes to observe the exotic quantum states with a purely geometric origin. In terms of basic physics, our finding provides useful insights into the nature of quantum states in the curved space. With respect to applications, our results suggest that wave-function collapse should be an important factor of consideration in designing and developing nanodevices, because curved geometry has become increasingly common in nanoscience and nanotechnology.

II. SCHRÖDINGER EQUATION ON A TRUNCATED CONIC SURFACE

The starting point in studying the quantum dynamics of a particle on a 2D curved surface is to derive the Schrödinger equation on the surface. A previous method was based on the idea of confining potential [1,2], where one starts from the Schrödinger equation in the 3D Euclidean space and applies some appropriate potential to constrain the particle motion to the curved surface. As a result, the Schrödinger equation constrained on a 2D curved surface defined by the metric tensor $g_{\mu\nu}$ can be written as [1,2]

$$-\frac{\hbar^2}{2M}\left[\frac{1}{\sqrt{g}}\partial_\mu(\sqrt{g}g^{\mu\nu}\partial_\nu)\right]\Psi + V_G\Psi = E\Psi, \tag{1}$$

where M is the particle mass, $g^{\mu\nu}$ is the contravariant component of $g_{\mu\nu}$, $g = \det g_{\mu\nu}$, and V_G is a scalar geometric potential given by

$$V_G = -\frac{\hbar^2}{2M}\left(K_m^2 - K\right), \tag{2}$$

where K_m and K are the mean and Gaussian curvatures of points on the surface, respectively, which characterize the internal and external geometric properties of the surface. Note that V_G has a pure geometric origin and it is independent of any externally applied potential (if any). The quantum properties of the normal mode χ_n in the perpendicular direction of the surface are governed by

$$-\frac{\hbar^2}{2M}\frac{\partial^2\chi_n}{\partial q_n^2} + V(q_n)\chi_n = E_n\chi_n, \tag{3}$$

where q_n is the coordinate normal to the surface and $V(q_n)$ is the confining potential that constrains the particle to the interface.

To be concrete, we consider the solution of the Schrödinger equation on a conic surface. A truncated cone can be obtained by a "cut-and-glue" process from a sheet of paper, as shown in Fig. 1. The distance away from the apex of the cone is denoted as $\rho \in [\rho_0, \infty)$, where the part of the cone with $\rho < \rho_0$ is removed. The truncation is physically infinitesimal in the sense that ρ_0 is chosen to be the size of one or two atoms, e.g., $\rho_0 \approx 2$ Å. The line element or metric on a truncated cone is

$$ds^2 = d\rho^2 + \alpha^2\rho^2 d\varphi^2, \tag{4}$$

where $\varphi \in [0, 2\pi)$ and $2\pi\alpha$ $(0 < \alpha < 1)$ is the sector angle of the corresponding solid angle of the cone. At $\rho = \rho_0$, there is a hard wall boundary condition: $\psi|_{\rho_0} = 0$, so the wave function does not extend into the forbidden region $\rho < \rho_0$. Since, as demonstrated in Appendix A, the geometric potential induced by the mean and Gaussian curvatures has a singularity at $\rho = 0$, the hard wall boundary condition at $\rho = \rho_0$ removes this singularity—a physically meaningful setting.

The Schrödinger Hamiltonian on a truncated conic surface becomes [8]

$$H = -\frac{\hbar^2}{2M}\left[\frac{1}{\rho}\frac{\partial}{\partial\rho}\left(\rho\frac{\partial}{\partial\rho}\right) + \frac{1}{\alpha^2\rho^2}\frac{\partial^2}{\partial\varphi^2}\right] + V_G, \tag{5}$$

where the geometry-induced potential is given by

$$V_G = -\frac{\hbar^2}{2M}\left(\frac{1-\alpha^2}{4\alpha^2\rho^2}\right). \tag{6}$$

Because of the circular symmetry of the conical geometric potential field, the angular momentum l is a good quantum number. The wave functions can thus be naturally written in terms of the angular momentum eigenstates $e^{il\varphi}$ as

$$\Psi(\mathbf{r}) = \psi(\rho)e^{il\varphi} \tag{7}$$

with $l = 0, \pm1, \cdots$ $(l \in \mathbb{Z})$. In the angular momentum representation, the Schrödinger equation reduces to the following radial equation:

$$\left[-\frac{\hbar^2}{2M}\frac{1}{\rho}\frac{d}{d\rho}\left(\rho\frac{d}{d\rho}\right) + U_G(\rho)\right]\psi(\rho) = E\psi(\rho), \tag{8}$$

where

$$U_G \equiv \frac{\hbar^2}{2M}\frac{\tilde{\nu}^2}{\rho^2} \tag{9}$$

with

$$\tilde{\nu}^2(\alpha, l) \equiv \frac{l^2}{\alpha^2} - \frac{1-\alpha^2}{4\alpha^2}. \tag{10}$$

The first term in Eq. (10) arises from the conical metric and the second term originates from the mean curvature of the cone, a quantum geometric potential.

Equations (9) and (10) indicate that, for zero angular momentum $l = 0$, the geometry-induced potential is attractive. In this case, bound states will naturally arise [8,48]. However, in spite of the attractive nature of the potential, a class of unusually extended or scattering states can emerge, and we will show below that they closely resemble the quantum states characteristic of atomic collapse (the main result of this paper). For nonzero angular momentum states $|l| \geqslant 1$, the potential is repulsive, so the resulting scattering states are of the conventional type.

To simplify notations, we transfer the term $\sqrt{2ME}\rho/\hbar$ into the dimensionless form $\sqrt{\epsilon}r$ with the requirement $\sqrt{2ME_0}\rho_0/\hbar \approx 1$, where $\epsilon \equiv E/E_0$ and $r \equiv \rho/\rho_0$. We assume M to be the electron mass and consider $E_0 = 1$ eV. The cutoff radial size is $\rho_0 = 1.93 \approx 2$ Å.

III. CHARACTERISTICALLY DISTINCT EIGENSTATES

Analytically solving Eqs. (8)–(10), we obtain three types of eigenstates: bound states and wave-function collapse states at zero angular momentum as well as conventional scattering states at finite angular momenta.

A. Bound states

For $l = 0$ and $E < 0$, the quantum particle is effectively under the inverse square attractive potential and will be confined around the origin. Using the general solution of the Bessel equation of the imaginary order and the imaginary argument [49]

$$\psi(\mathbf{r}) = AK_{i\nu}(x) + BL_{i\nu}(x), \tag{11}$$

and considering the divergence of function $L_{i\nu}(x)$ at infinity, we have that the solutions of the Schrödinger equation for $r \geqslant 1$ and $\alpha \in (0,\ 1)$ are non-normalized bound states, which can be written as

$$\psi_{0,\epsilon_n}(\mathbf{r}) = K_{i\tilde{\alpha}}\big(\sqrt{-\epsilon_n}r\big), \tag{12}$$

where the new notation

$$\tilde{\alpha} \equiv \sqrt{1-\alpha^2}/(2\alpha)$$

is introduced to emphasize the imaginary order of the Bessel functions for zero angular momentum. Applying the boundary condition, we have that the zeros of $K_\nu(x)$ determine the discrete energy spectrum. In particular, at $\rho = \rho_0$ or $r = 1$, applying the hard wall boundary condition leads to

$$K_{i\tilde{\alpha}}\big(\sqrt{-\epsilon_n}\big) = 0. \tag{13}$$

Figure 2 shows the zeros of the function $K_{i\tilde{\alpha}}(\sqrt{-\epsilon})$. For $\sqrt{-\epsilon} \to 0$, we have [49]

$$K_{i\tilde{\alpha}}\big(\sqrt{-\epsilon}\big) \to \sin[\tilde{\alpha}\ln(\sqrt{-\epsilon}/2) - \phi_{\tilde{\alpha},0}] = 0, \tag{14}$$

where $\phi_{\tilde{\alpha},0} = \arg\{\Gamma(1+i\tilde{\alpha})\}$ and Γ is the gamma function. The dimensionless eigenenergy spectrum is given by

$$\epsilon_n \approx -4\exp\left[2(-n\pi + \phi_{\tilde{\alpha},0})/\tilde{\alpha}\right], \tag{15}$$

where for $\alpha \in [0.15, 1)$ we have $n \in N^+$ and the ground state corresponds to $n_0 = 1$, while for $\alpha \in (0, 0.15)$ the approximation in Eq. (14) is invalid due to the increasing value of the ground-state energy. In this case, the minimal integer n_0 is less than 1 and the ground-state energy ϵ_{n_0} is smaller than the approximate value. For $\alpha \in (0, 1)$, the whole eigenenergy spectrum ϵ_n goes from a finite negative value to 0^-. Since $\sqrt{-\epsilon} = \sqrt{-2ME}\rho_0/\hbar$, the corresponding bound-state energy spectrum becomes

$$E_n \approx \frac{\hbar^2\epsilon_n}{2M\rho_0^2}, \tag{16}$$

which is consistent with the result in Refs. [8,48] with the approximation $\phi_{\tilde{\alpha},0}/\tilde{\alpha} \approx -\gamma$, where γ is the Euler constant. There are then an infinite number of bound states.

For $\alpha = 1/6$, the maximal zero root of $K_{i\tilde{\alpha}}(\sqrt{-\epsilon})$ occurs at $n = 1$, which corresponds to the ground state. The difference in the energy level decreases as n increases from 1 to ∞. Since the function $K_{i\tilde{\alpha}}(\sqrt{-\epsilon})$ exhibits infinite oscillations near the zero energy point, as shown in Fig. 2(a), there are an infinite number of bound states the energy spectrum of which converges to zero 0^-, near which the spectrum is quasi-continuous, corresponding to the semiclassical regime. In the vicinity of the virtual zero root (corresponding to $n = 0$), the asymptotic behavior of $K_{i\tilde{\alpha}}(\sqrt{-\epsilon})$ is approximately exponential. For $r \to \infty$, we have

$$K_{i\tilde{\alpha}}\big(\sqrt{-\epsilon_n}r\big) \sim \sqrt{\frac{\pi}{2\sqrt{-\epsilon_n}r}}e^{-\sqrt{-\epsilon_n}r}. \tag{17}$$

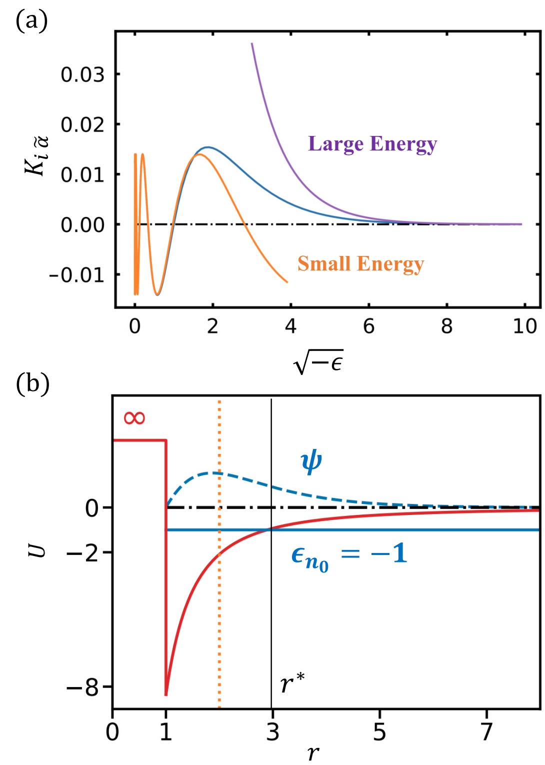

FIG. 2. Bound states for $\alpha = 1/6$. (a) The bound states determined by the zeros of the function $K_{i\tilde{\alpha}}$ (the middle curve), the asymptotic behaviors of which in the small and large energy regimes are given by $\sin[\tilde{\alpha}\ln(x/2) - \phi_{\tilde{\alpha},0}]$ (the oscillatory curve for a small energy) and $e^{-x}/\sqrt{x}$ (the upper curve for a large energy), respectively, where $x = \sqrt{-\epsilon}$. (b) The ground-state wave function (dashed curve) with the energy $\epsilon_{n_0} = -1$ (the solid horizontal line) for the potential of the form $-\hbar^2\tilde{\alpha}^2/(2M\rho_0^2r^2)$ (solid trace) for $r \geqslant 1$. There is a hard wall at $r = 1$. The depth of the potential well, the minimal potential for the whole region, is about $U \approx -8$. The vertical dotted line denotes the "center of mass" $\langle r\rangle$ of the wave function, which is to the left of r^*, the classical forbidden region. All quantities plotted are dimensionless.

Figure 2(b) shows, for $\alpha = 1/6$, the wave function of the ground state of energy $\epsilon_{n_0} = -1$. Using Eq. (16) and considering that ϵ_n is independent of ρ_0, we have $E_{n_0} \to -\infty$ for $\rho_0 \to 0$. In this case, the ground state corresponds to the classical picture of the falling of the particle into the center as $\rho_0 \to 0$ (an analogous situation was discussed by Landau [10]). In principle, for $\rho_0 \to 0$, all bound states with a finite energy correspond to classical trajectories falling to the center (to be analyzed in Sec. V).

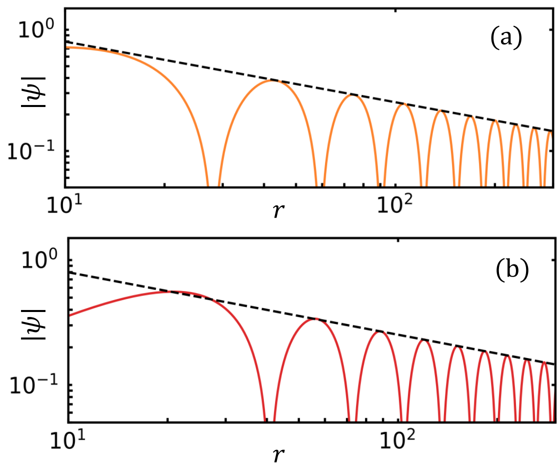

FIG. 3. Normalization of the quantum states at large distances from the conical apex: (a) a collapse state at zero angular momentum ($l = 0$ and $E > 0$) and (b) a conventional scattering state at a finite angular momentum ($|l| > 0$ and $E > 0$). The dimensionless distance is defined as $r \equiv \rho/\rho_0$ (Sec. II).

B. Scattering states with geometry-induced wave-function collapse

For $l = 0$ and $E > 0$, a particle on the truncated conic surface experiences an equivalent inverse square attractive potential as for the case of bound states discussed in Sec. III A. In this case, the solutions are scattering states that exhibit infinite oscillations with energy near the zero energy point. In particular, using the general solution of the Bessel equation of the imaginary order and the real argument [49], we write the real solution for $r \geqslant 1$ and $\alpha \in (0,\ 1)$ as

$$\psi_{0,\epsilon}(\mathbf{r}) = AF_{i\tilde{\alpha}}(\sqrt{\epsilon}r) - BG_{i\tilde{\alpha}}(\sqrt{\epsilon}r), \tag{18}$$

where the functions $F_{i\tilde{\alpha}}$ and $G_{i\tilde{\alpha}}$ are linear combinations of Hankel's functions of the first and second kind [given by Eqs. (B9) and (B10) in Appendix B, respectively], and the coefficients $0 \leqslant A \leqslant 1$ and $0 \leqslant B \leqslant 1$ are

$$A = \frac{G_{i\tilde{\alpha}}(\sqrt{\epsilon})}{\sqrt{G^2_{i\tilde{\alpha}}(\sqrt{\epsilon}) + F^2_{i\tilde{\alpha}}(\sqrt{\epsilon})}},\qquad B = \frac{F_{i\tilde{\alpha}}(\sqrt{\epsilon})}{\sqrt{G^2_{i\tilde{\alpha}}(\sqrt{\epsilon}) + F^2_{i\tilde{\alpha}}(\sqrt{\epsilon})}}. \tag{19}$$

The solution in Eq. (18) satisfies the boundary condition $\psi|_{r=1} = 0$ and extends to infinity with proper normalization, as shown in Fig. 3(a). For $r \to \infty$, the functions $F_{i\tilde{\alpha}}(\sqrt{\epsilon}r)$ and $G_{i\tilde{\alpha}}(\sqrt{\epsilon}r)$ tend to the conventional Bessel's functions:

$$J_0(\sqrt{\epsilon}r) \approx \sqrt{\frac{2}{\pi\sqrt{\epsilon}r}}\cos\left(\sqrt{\epsilon}r - \frac{\pi}{4}\right), \tag{20}$$

$$J_1(\sqrt{\epsilon}r) \approx \sqrt{\frac{2}{\pi\sqrt{\epsilon}r}}\sin\left(\sqrt{\epsilon}r - \frac{\pi}{4}\right), \tag{21}$$

respectively (Appendix B). Numerically, we find that for $\alpha \in [2/6, 1)$ the asymptotic forms hold for $\sqrt{\epsilon}r > 5$. For $\alpha < 2/6$, the asymptotic forms are valid for somewhat larger values of $\sqrt{\epsilon}r$. For $\alpha \in (0, 1)$ and fixed r, we have the following asymptotic forms [49] of $F_{i\tilde{\alpha}}(\sqrt{\epsilon}r)$ and $G_{i\tilde{\alpha}}(\sqrt{\epsilon}r)$ for $\epsilon \to 0$:

$$F_{i\tilde{\alpha}}(\sqrt{\epsilon}r) \sim \cos[\tilde{\alpha}\ln(\sqrt{\epsilon}r/2) - \phi_{\tilde{\alpha},0}], \tag{22}$$

$$G_{i\tilde{\alpha}}(\sqrt{\epsilon}r) \sim \sin[\tilde{\alpha}\ln(\sqrt{\epsilon}r/2) - \phi_{\tilde{\alpha},0}], \tag{23}$$

where $\phi_{\tilde{\alpha},0} = \arg\{\Gamma(1 + i\tilde{\alpha})\}$ and Γ is the gamma function. For $\epsilon \to 0$, the scattering states given by Eq. (18) thus have the following form:

$$\frac{A\sin[\tilde{\alpha}\ln(r)]}{\sqrt{B - C\cos^2[\tilde{\alpha}\ln(\sqrt{\epsilon}/2) - \phi_{\tilde{\alpha},0}]}}, \tag{24}$$

where $r \geqslant 1$, $A = -\sqrt{2/(\tilde{\alpha}\pi)}$, $B = \coth(\tilde{\alpha}\pi/2)$, and $C = 2/\sinh(\tilde{\alpha}\pi)$. In this near zero energy regime, the wave function thus oscillates with the period $2\pi/\tilde{\alpha}$ in a natural logarithmic scale. The resulting abnormal scattering states are effectively collapse states, corresponding to classically collapsing trajectories (see Sec. V).

C. Scattering states with finite angular momentum

For a nonzero angular momentum, $l \neq 0$, the overall inverse square potential [Eq. (9)] is repulsive, so the scattering states are conventional with a positive energy. The general solution of the Bessel equation of real order with a real argument is

$$\psi(\mathbf{r}) = AJ_\nu(x) + BY_\nu(x) \tag{25}$$

so the scattering states for the whole energy region can be written as

$$\psi_{l,\epsilon}(\mathbf{r}) = [AJ_{\tilde{\nu}}(\sqrt{\epsilon}r) - BY_{\tilde{\nu}}(\sqrt{\epsilon}r)]e^{il\varphi}, \tag{26}$$

for $l = \pm1, \pm2, \ldots$, where the coefficients $0 \leqslant A \leqslant 1$ and $0 \leqslant B \leqslant 1$ are given by

$$A = \frac{Y_{\tilde{\nu}}(\sqrt{\epsilon})}{\sqrt{J^2_{\tilde{\nu}}(\sqrt{\epsilon}) + Y^2_{\tilde{\nu}}(\sqrt{\epsilon})}},\qquad B = \frac{J_{\tilde{\nu}}(\sqrt{\epsilon})}{\sqrt{J^2_{\tilde{\nu}}(\sqrt{\epsilon}) + Y^2_{\tilde{\nu}}(\sqrt{\epsilon})}}, \tag{27}$$

and the order of Bessel functions has the form

$$\tilde{\nu}(\alpha, l) = \sqrt{\frac{l^2}{\alpha^2} - \frac{1-\alpha^2}{4\alpha^2}} \tag{28}$$

with $\alpha \in (0, 1)$. Equation (26) is the exact analytical solution, where $Y_{\tilde{\nu}}(\sqrt{\epsilon}r)$ diverges at the boundary $r = 1$ for $\epsilon \approx 0$. In numerical simulations, we set the maximum cutoff as $Y_{\tilde{\nu}} \leqslant 100$, guaranteeing the hard wall boundary condition at $r = 1$. The maximal error of the LDOS is of the order of 10^{-32} near the zero energy point and in the finite energy region (0,10]. Asymptotically, as shown in Fig. 3(b), the conventional scattering states can be normalized at infinity through the standard form

$$J_{\tilde{\nu}}(\sqrt{\epsilon}r) \sim \sqrt{\frac{2}{\pi\sqrt{\epsilon}r}}\cos\left(\sqrt{\epsilon}r - \frac{\tilde{\nu}\pi}{2} - \frac{\pi}{4}\right),$$
$$Y_{\tilde{\nu}}(\sqrt{\epsilon}r) \sim \sqrt{\frac{2}{\pi\sqrt{\epsilon}r}}\sin\left(\sqrt{\epsilon}r - \frac{\tilde{\nu}\pi}{2} - \frac{\pi}{4}\right). \tag{29}$$

We discuss two extreme cases among the three kinds of quantum states: $\alpha \to 1$ and $\alpha \to 0$. For $\alpha \to 1$ with fixed ρ_0, the conic surface becomes a 2D plane with a hole of radius ρ_0 at the center. The geometric potential vanishes because $\tilde{\alpha}^2 = (1-\alpha^2)/(4\alpha^2) = 0$. In this case, the bound states disappear due to the zero depth of the potential well in the form of $\hbar^2\tilde{\alpha}^2/(2M\rho_0^2 r^2)$, which is defined by the minimum of the effective potential. The geometry-induced collapse states and scattering states with finite angular momenta degenerate into the normal scattering states in the plane, which can be expressed as a linear combination of $J_l(\sqrt{\epsilon}r)$ and $Y_l(\sqrt{\epsilon}r)$ multiplied by $e^{il\varphi}$ for $l = 0, \pm1, \pm2, \ldots$ with

$$\lim_{\tilde{\alpha}\to 0} F_{i\tilde{\alpha}} \to J_0(\sqrt{\epsilon}r),$$
$$\lim_{\tilde{\alpha}\to 0} G_{i\tilde{\alpha}}(\sqrt{\epsilon}r) \to Y_0(\sqrt{\epsilon}r),$$

which have been verified numerically and are consistent with, e.g., Eq. (3.3) in Ref. [49] and $\tilde{\nu} \to l$. For $\alpha \to 0$ with fixed ρ_0, the conic surface tends to a cylindrical one with an infinitesimally small radius. In this case, since $\tilde{\alpha} \to \infty$, the geometric potential is homogeneously infinite for the whole surface region. Because the potential is infinitely negative for zero angular momentum and infinitely positive for nonzero angular momenta, the wave functions simply vanish.

IV. LOCAL DENSITY OF STATES AND DEMONSTRATION OF COLLAPSE STATES

In general, the characteristics of the wave function depend on the distance from the apex of the cone r and the sector angle of a truncated cone as measured by $2\pi\alpha$, which can be studied through the LDOS. The general definition of the LDOS [32] is

$$N(\epsilon, \mathbf{r}) = \sum_{\epsilon'} |\Psi_{\epsilon'}(\mathbf{r})|^2 \delta(\epsilon - \epsilon') = \sum_{l=-\infty}^{+\infty} n_l(\epsilon, \mathbf{r}), \tag{30}$$

where $n_l(\epsilon, \mathbf{r}) = |\psi_{l,\epsilon}(\mathbf{r})|^2$, a quantity that involves only the positive-energy states. Evidence of the emergence of the collapse states is presented in Figs. 4(b)–4(d) for $\alpha = 5/6$, 4/6, and 3/6, respectively, where the infinite oscillations of the LDOS are shown in the corresponding insets. Note that, for $\alpha = 3/6$, LDOS oscillations can be seen in a relatively large energy region: $E \approx \mu$eV (corresponding roughly to the accessible resolution in the current experimental technology [50]). The results indicate that zero energy is the accumulation point of infinitely many resonances, a characteristic of the atomic collapse states [7,29,32]. The collapse states arise from the conic surface for α values close neither to one nor to zero, as the energy interval in which the LDOS oscillations are pronounced shrinks to zero for $\alpha \to 1$ and the LDOS is zero for $\alpha \to 0$.

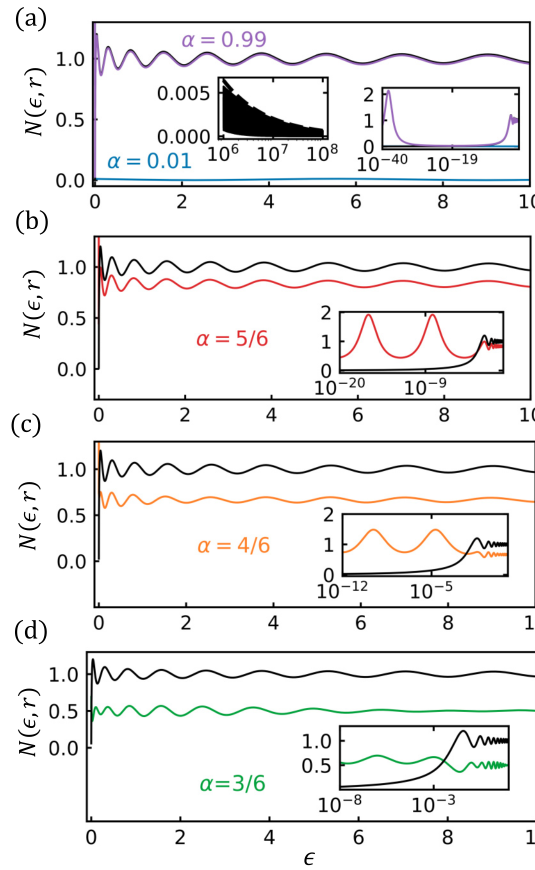

FIG. 4. Behavior of the total LDOS for different conic surfaces at $r = 10$. (a) LDOS for the two extreme cases: $\alpha = 0.99$ and 0.01 (the solid curves and the right inset for small energy). For $\alpha = 0.99$, the LDOS oscillates about the value 1, a characteristic of the normal scattering states for $\alpha = 1$ in the 2D plane with a hole of radius ρ_0. For $\alpha = 0.01$, no quantum states exist to contribute to the LDOS. In a higher-energy regime, the asymptotic behavior of the LDOS for $\alpha = 1$ is shown in the left inset. [(b)–(d)] LDOS plots for $\alpha = 5/6$, 4/6, and 3/6, respectively, where the top curve in each panel is for $\alpha = 1$. In these cases, the values about which the LDOS oscillates are between zero and one. In a small energy interval near zero, the LDOS exhibits infinite oscillations with the energy, as shown in the respective insets of the three cases. As argued in the text, in a near zero energy interval, the main contribution to the LDOS comes from the zero angular momentum states, where the infinite oscillations are indicative of the collapse nature of these states. In each panel, the dimensionless energy ϵ is defined as $\epsilon \equiv E/E_0$ (Sec. II).

For large energy $\epsilon \to \infty$, according to Eqs. (26), (27), and (29), the norm square of the conventional scattering states with fixed angular momenta can be written as

$$\lim_{\epsilon\to\infty} |\psi_{l,\epsilon}|^2 \to \frac{2}{\pi\sqrt{\epsilon}r}\sin^2[\sqrt{\epsilon}(1-r)], \tag{31}$$

which is independent of the angular momentum quantum number l because of the asymptotic relations:

$$A \to \sin\left(\sqrt{\epsilon} - \tfrac{\tilde{\nu}\pi}{2} - \tfrac{\pi}{4}\right),$$
$$B \to \cos\left(\sqrt{\epsilon} - \tfrac{\tilde{\nu}\pi}{2} - \tfrac{\pi}{4}\right)$$

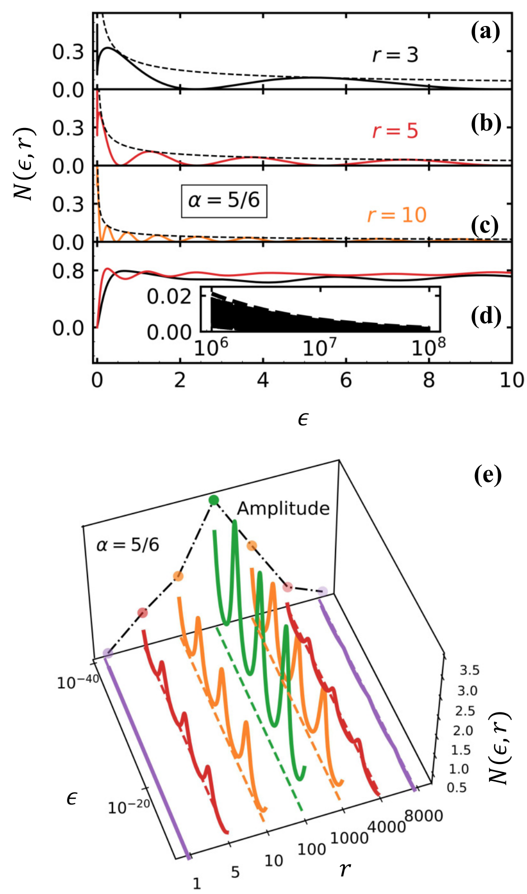

FIG. 5. Contributions to the LDOS from the collapse and conventional scattering states. [(a)–(c)] The contribution from the collapse states for three distance values with the asymptotic behavior (dashed curves) in a large energy interval. (d) The contribution from the conventional scattering states at two distances: $r = 3$ and 5. The inset shows the decay behavior in the higher-energy regime for $r = 3$, where the dashed curve indicates the asymptotic behavior. (e) Oscillations of the LDOS due to the collapse states in a small near zero energy interval for different values of the distance, as represented by a 3D plot of the LDOS in terms of both the energy and distance. The amplitudes of LDOS oscillations for different distances are projected to the 2D plane. All quantities plotted are dimensionless.

with $\epsilon \to \infty$. The asymptotic LDOS of the conventional states for large energies is thus proportional to N_l: LDOS $\propto N_l \lim_{\epsilon\to\infty} |\psi_{l,\epsilon}|^2$. For $l \in [-50, 0) \cup (0, 50]$, we have $N_l = 100$ for conventional scattering states, as shown in the inset of Fig. 5(d). For $l \in [-50, 50]$, we have $N_l = 101$ to include the degenerate collapse states for α close to 1, as shown in the inset of Fig. 4(a). For the collapse states with $\alpha \in (0, 1)$, the asymptotic LDOS has the form $2/(\pi\sqrt{\epsilon} r)$, as shown in Figs. 5(a)–5(c) and 6(a) based on Eqs. (19), (20) and (21).

As α decreases from one to zero, the value around which the total LDOS oscillates reduces from one to zero, as shown in Figs. 4(a)–4(d). The main reduction comes from the conventional scattering states shown in Figs. 6(a) and 6(b). This can be argued heuristically, as follows. For a fixed distance from the conical apex, the wave functions $F_{i\tilde{\alpha}}(\sqrt{\epsilon} r)$ and $G_{i\tilde{\alpha}}(\sqrt{\epsilon} r)$ for the sufficiently large energy, e.g., $\sqrt{\epsilon} r > 5$, tend to J_0 and J_1, respectively, regardless of the values of α. Consequently, the reduction does not occur for the collapse states, as shown in Fig. 6(a). For the conventional scattering states, given a finite energy interval, the high angular momentum states $J_{\tilde{\nu}}(\sqrt{\epsilon} r)$ will be pushed out of this energy interval into a higher-energy region, leaving behind the low angular momentum states to contribute to the total LDOS, as shown in Fig. 6(b). As a result, the value around which the LDOS oscillates will reduce with α. In the extreme case of α decreasing to zero, the number of contributing states becomes zero.

To obtain a more comprehensive picture of the contribution of the collapse states to the LDOS, we decompose it into two parts:

$$N(\epsilon, \mathbf{r}) = \sum_{l=0} \bar{n}_l(\epsilon, \mathbf{r}) + \sum_{l\neq 0} n_l(\epsilon, \mathbf{r}), \tag{32}$$

where the first and second terms are the contributions from the collapse states and the conventional scattering states, respectively. As an example, we fix $\alpha = 5/6$ and examine the two types of contribution at different distances from the apex of the cone. Figures 5(a)–5(c) show the contribution to the LDOS from the collapse states for three distance values, respectively, while Fig. 5(d) displays the contribution from the conventional scattering state at two distances. The oscillations of the collapse-state-contributed LDOS near the zero energy point with the distance exhibit a different behavior, as shown in a 3D plot of $N(\epsilon, r)$ versus the energy and distance, as exemplified in Fig. 5(e). In this interval of infinitesimal energies, the oscillation amplitude of $N(\epsilon, r)$ depends on the distance r in the form of $\sin(\tilde{\alpha} \ln r)$ as in Eq. (24), described by the 2D projection in the 3D plot of Fig. 5(e). The oscillation frequency depends on α as determined by

$$\cos^2[\tilde{\alpha} \ln \sqrt{\epsilon} + C(\tilde{\alpha})],$$

providing an explanation of the observed same number of periods of oscillation at different distances for the same energy range, as shown in Fig. 5(e).

What is the effect of varying the sector angle $2\pi\alpha$ of the truncated cone on the LDOS? Figures 6(a) and 6(b) show, for fixed $r = 5$ and several values of α, the LDOS versus the energy for the contributions from the collapse and conventional scattering states, respectively. In both cases, the number of oscillation periods is independent of the value of α, as can be seen from Eqs. (20), (21), and (31). In an infinitesimal energy interval near zero, Eq. (24) stipulates that the oscillation amplitude of the LDOS associated with the collapse states enhances with α but the oscillation frequency reduces, as shown in Fig. 6(c). For a near zero α value, e.g., $\alpha = 0.01$, the oscillation amplitude is approximately zero. In the opposite extreme case, e.g., $\alpha = 0.99$, the LDOS exhibits a single oscillation and then approaches zero.

To be concrete, we define the average LDOS with respect to energy values near the zero energy point $\epsilon \approx 0$. In this energy interval, the LDOS is mainly contributed to by the geometry-induced collapse states, which exhibits regular oscillations as stipulated by Eq. (24). The average LDOS is

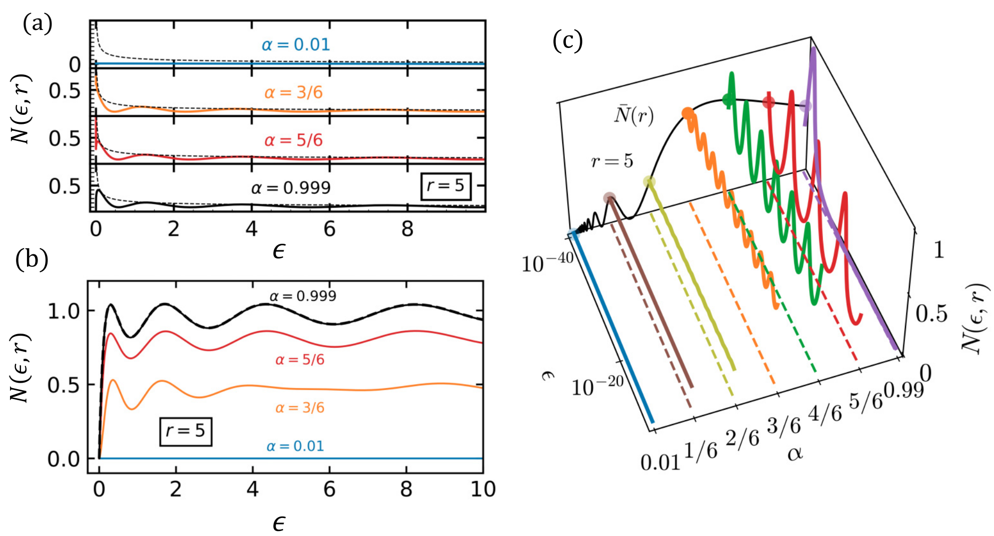

FIG. 6. Effect of different conic geometry on the LDOS. [(a), (b)] LDOS vs energy contributed to by the collapse and conventional scattering states, respectively, for $r = 5$ and four different values of the sector angle $2\pi\alpha$. The dashed curves in (a) show the asymptotic behaviors in the high-energy region. The dashed curve in (b) show the LDOS of the conventional scattering states in the 2D plane with a hard hole. (c) The LDOS contributed to by the collapse states in an infinitesimal energy interval near zero, the frequencies of which decrease while the amplitudes increase as α increases from zero to one. The average LDOS $\bar{N}(r)$ over the near zero energy point is plotted vs α, which is projected to the 2D plane. The solid curve in the back plane is the prediction of Eq. (34) and the data points are the corresponding numerical results. All quantities plotted are dimensionless.

given by

$$\bar{N}(r) = \{\max[N(\epsilon, r)] + \min[N(\epsilon, r)]\}/2. \tag{33}$$

The 2D projection of the 3D plot in Fig. 6(c) shows the average value of the LDOS, where the black curve represents the theoretical formula obtained from Eq. (24):

$$\bar{N}(r) = \frac{1}{2}\left[\frac{1}{B} + \frac{1}{B-C}\right]A^2 \sin^2 [\tilde{\alpha} \ln (r)], \tag{34}$$

where A, B, and C are defined by Eq. (24), which only depend on $\tilde{\alpha}$. The data points in Fig. 6(c) are from numerical simulations, which fall precisely on the theoretical curve.

V. A CLASSICAL PICTURE

To gain deep physical insights into the geometry-induced collapsed states, we construct the corresponding classical picture, following the pioneering work on geometric potential [6,7]. Consider a classical particle of mass M moving on a 2D truncated conic surface, subject to an external potential. The effective classical potential is $-L_{\mathrm{eff}}^2/(2M\rho^2)$, where L_{eff} is the coefficient. The classical Hamiltonian is

$$H = \frac{|\mathbf{p}|^2}{2M} - \frac{L_{\mathrm{eff}}^2}{2M\rho^2}. \tag{35}$$

The particle is constrained to move in the region $\rho > \rho_0$ with a hard wall at $\rho = \rho_0$. The classical linear momentum can be decomposed into two parts, the radial and angular components, as

$$|\mathbf{p}|^2 = p_\rho^2 + L_z^2/(\alpha^2\rho^2), \tag{36}$$

where $L_z = \alpha\rho p_\varphi$ is the classical angular momentum characterizing the particle motion around the z axis. Since the potential $-L_{\mathrm{eff}}^2/(2M\rho^2)$ results in a central force field, the angular momentum L_z is conserved. The classical Hamiltonian can be expanded as

$$H = \frac{p_\rho^2}{2M} + \frac{1}{2M\rho^2}\left(\frac{L_z^2}{\alpha^2} - L_{\mathrm{eff}}^2\right), \tag{37}$$

where the quantities in the bracket of the second term are constants, so this term is effectively a potential function of ρ. Depending on L_z and L_{eff}, this effective potential can be either positive or negative. The radial motion of the particle is thus completely governed by the Hamiltonian (37).

For $|L_{\mathrm{eff}}| > |L_z|/\alpha$, the second term in Eq. (37) is negative and the attractively effective potential. For total negative energy $E < 0$, the particle is trapped inside the region with radius $\rho \in (\rho_0, \rho^*)$, where $p_\rho(\rho^*) = 0$, as shown in Fig. 7(a). The particle spirals inward and reflects from the hard wall boundary at ρ_0, spirals outward, is pulled back by the attractive potential, begins to spiral inward again, and so on, as depicted in Fig. 7(d). This type of motion corresponds to the bound states in the quantum regime.

For $E > 0$, in the $\rho \to \infty$ limit, there is a radial kinetic energy of the form $p_\rho^2/(2M)$. In this case, ρ^* extends to infinity. As illustrated in Figs. 7(b) and 7(e), the particle spirals inward toward the center from infinity, is reflected at the boundary ρ_0, and then spirals outward back to infinity. This is the classical picture of the geometry-induced collapse state with an infinitely oscillating local density of states.

For $|L_{\mathrm{eff}}| < |L_z|/\alpha$, the second term in Eq. (37) is positive and the repulsively effective potential. The motion of the particle is constrained in the region $\rho \in (\rho^*, \infty)$. As illustrated in Figs. 7(c) and 7(f), it is not a falling trajectory and the particle is scattered away from ρ^*, corresponding to the conventional

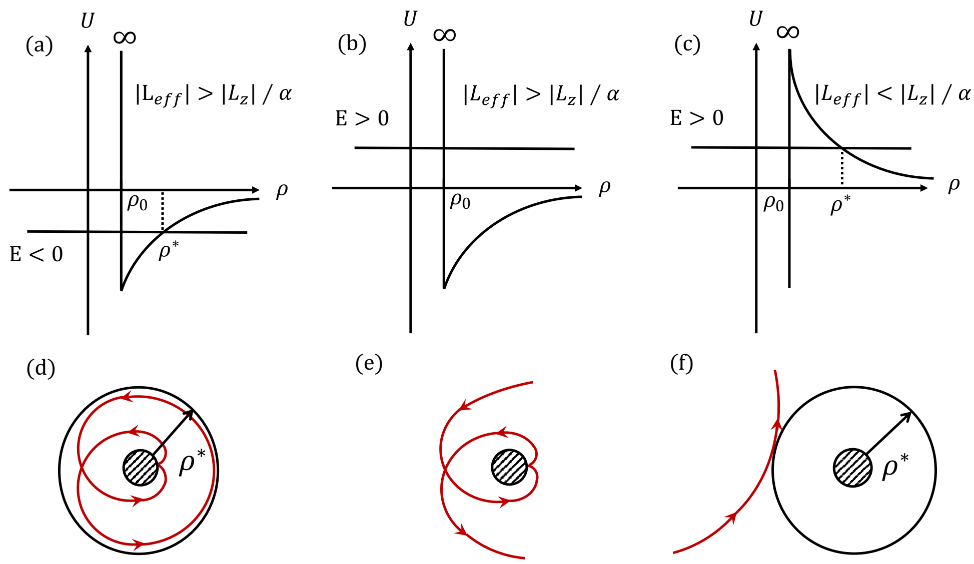

FIG. 7. Representative classical particle trajectories on a truncated conic surface from the Hamiltonian (35). [(a)–(c)] Three different potential profiles, and [(d)–(f)] the corresponding classical trajectories. [(a), (d)] For $|L_{\rm eff}| > |L_z|/\alpha$ and $E < 0$, the effective potential is attractive and the particle is confined in the region (ρ, ρ^*), corresponding to bound states. [(b), (e)] For $|L_{\rm eff}| > |L_z|/\alpha$ and $E > 0$, the classical particle can collapse to ρ_0 in finite time but would eventually escape to infinity due to the reflective boundary condition at ρ_0. Geometry-induced wave-function collapse occurs in this case. [(c), (f)] For $|L_{\rm eff}| < |L_z|/\alpha$ and $E > 0$, the effective potential is repulsive and the particle is confined in the region (ρ^*, ∞), corresponding to the conventional quantum scattering case.

quantum scattering states. Note that ρ_0 is assumed to be sufficiently small so that the potential at $\rho = \rho_0$ can be regarded as infinite. Furthermore, if we quantify L_z as $l\hbar$ following the standard procedure of quantization and assume $L_{\rm eff}$ is equivalent to $\hbar\tilde{\alpha}$ in the quantum-classical correspondence, the effective potential in Eq. (37) will have the same mathematical form as Eqs. (9) and (10).

VI. EXPERIMENTAL FEASIBILITY OF OBSERVING THE GEOMETRY-INDUCED COLLAPSE STATES

We analyze in detail the feasibility of observing the phenomenon of geometry-induced wave-function collapse. A basic issue is to measure the LDOS oscillations associated with the collapse phenomenon. With the development of the scanning tunneling microscopy (STM) technology [51,52], the LDOS can be detected by STM with tunneling current proportional to the LDOS of the surface at the position of the tip [19,53,54]. For example, a recent experimental work [50] reported the achievement of a μeV tunneling resolution with *in operando* measurement capabilities of STM, making it feasible to observe the oscillations in the LDOS associated with the collapse state, as shown in Fig. 8(a), where the dimensional energy is about ϵ eV (defined below).

Since the experimental observation of atomic collapse was primarily achieved in graphene [19,36–39], we analyze the feasibility of experimentally observing the phenomenon of geometry-induced wave-function collapse in graphene. However, our theoretical prediction of this phenomenon has been made through the solutions of the Schrödinger equation on a curved surface, so for graphene a critical issue is band-gap opening. To carry out the analysis, we first recall some basic parameters in our calculation of the LDOS of the Schrödinger electron: the rest mass energy is $Mc^2 \approx 0.511$MeV and the radial cutoff size on a conic surface is $\rho_0 \approx 2$ Å. In the dimensionless form, we have $\sqrt{2ME_0}\rho_0/\hbar \approx 1$ by setting $E_0 \approx 1$ eV.

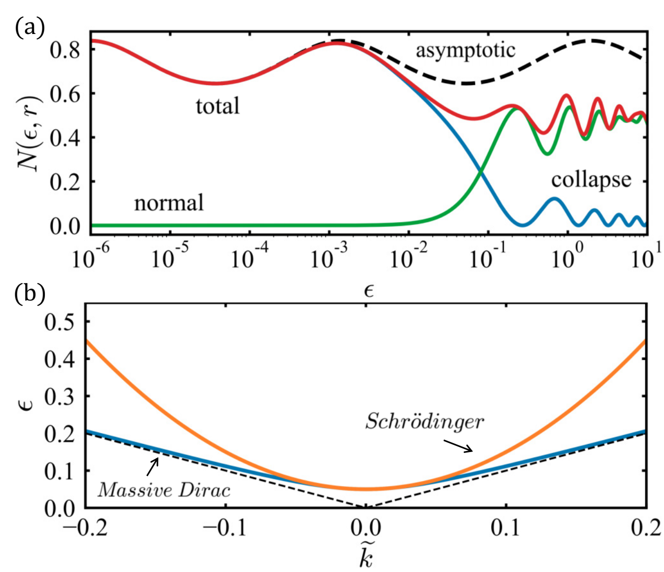

FIG. 8. Feasibility of experimentally observing geometry-induced wave-function collapse through LDOS oscillations. (a) For the sector angle $2\pi\alpha = \pi$ of the truncated cone, LDOS oscillations associated with total, collapse, and normal states with the corresponding behavior near zero energy, where $\epsilon \in [10^{-6}, 10^{-3}]$ corresponds to $\Xi \in 2 \times [1, 10^3]$ μeV. Experimental observation of the oscillations is feasible [55,56] (see text for an analysis). (b) The energy-momentum dispersion relation of a massive Dirac fermion and a Schrödinger particle with the dimensionless energy gap $\widetilde{\Delta} = 0.05$, corresponding to $\Delta = 0.1$ eV.

As reported in Ref. [57], band-gap opening can be realized around 0.26 eV in graphene through epitaxial growth on the SiC substrate, where the gap decreases as the sample thickness increases. It is thus experimentally feasible to set the band gap to be $\Delta \approx 0.1$eV, which is related to the effective mass of the quasiparticle as $\Delta = M^* v_F^2$. The energy-momentum dispersion relation of a massive Dirac fermion measured from a Dirac point in dimensionless form can be written as

$$\epsilon = \sqrt{\widetilde{k}^2 + \widetilde{\Delta}^2}, \tag{38}$$

where $\epsilon = \Xi/\Xi_0$, $\widetilde{k} = \hbar v_F k/\Xi_0$, and $\widetilde{\Delta} = \Delta/\Xi_0$. Because of the effective mass M^*, it is necessary to transform the original characteristic quantity into a different form, i.e.,

$$\sqrt{2ME_0}\rho_0/\hbar = \sqrt{2M^*\Xi_0}\xi_0/\hbar \approx 1 \tag{39}$$

with the new energy unit Ξ_0 and cutoff radius ξ_0. In the limit of a large gap, $\widetilde{\Delta} \gg \widetilde{k}$, the dispersion relation can be approximated as

$$\epsilon \approx \widetilde{\Delta} + \delta\epsilon,$$

where $\delta\epsilon \equiv \widetilde{k}^2/(2\widetilde{\Delta})$. This is the dispersion relation for a Schrödinger particle.

Next, we describe the process required for fabricating a graphene cone and articulate the possibility of realizing a truncated graphitic cone at the nanoscale (the setting of our theoretical analysis and computations). Graphitic cones (or graphene [58]) were first reported in Ref. [55] in 1997 with the disinclination defects that are multiples of 60°, which correspond to a given number of pentagons: disk (no pentagons), five types of cones (one to five pentagons), and open tubes (six pentagons). Another cone-helix structure with a wide distribution of apex angles in the cone's cross section was experimentally realized [59]. In a very recent experimental study [60], spiral graphite cones have been successfully grown under normal conditions without requiring high temperatures and high pressure. In addition, open graphitic cones with an apex angle, e.g., 60° (lampshade structures), were realized [56]. Based on these current experimental achievements, we conclude that it is feasible to fabricate a nanotruncated graphene cone with an open gap.

According to the dimensionless form Eq. (39), the radial cutoff size of a truncated graphite cone can be set as $\xi_0 = 5\rho_0 \approx 1$ nm, so the characteristic energy is $\Xi_0 = 2E_0 = 2$ eV with the energy band gap $\Delta \approx 0.1$ eV. From our theoretical results, if the graphite cone is shaped as $\alpha = 0.5$ (so the apex of the cone is 60° as reported in Refs. [55,56]) and if the LDOS is to be detected at the radial position $\rho = r\xi_0 \approx 6$nm, where $r = \exp[\pi/(2\alpha)] \approx 6$, it would be possible to observe the collapse oscillations of the LDOS with the energy interval $\Xi = \delta\epsilon\,\Xi_0 \in 2 \times [1, 10^3]$ μeV. In this case, the wave vector is

$$\widetilde{k} \approx \sqrt{2\delta\epsilon\widetilde{\Delta}} \approx [10^{-3.5}, 10^{-2}],$$

which is describable by the Schrödinger equation, as shown in Fig. 8(b).

Our analysis of the experimental feasibility indicates that the phenomenon of geometry-induced wave-function collapse can arise in nanoscale graphene systems, rendering it important to take this phenomenon into consideration when developing graphene-based devices that involve curved or Riemannian geometry.

VII. DISCUSSION

Our paper has focused on the quantum states of particles confined on a truncated conic surface, for which the corresponding geometric potential has the form of inverse squared distance. It has been established for a long time that, semiclassically, this type of potential in three dimensions can cause a particle to collapse to the center [9,10,17,18]. The main reason that we chose to study the conic structure is that it can be realized in experiments, such as graphite nanocones [55,59,61,62] where the issue of topological phase [63–66] was addressed [58,67–73]. There were also previous studies [8,23–26] on the effects of the geometric potential in terms of the mean and Gaussian curvatures [8,24] on the quantum states on the conic surface. The main contribution of our paper is the finding of a class of quantum states that mimic those arising in atomic collapse, but here the collapse mechanism is purely geometrical, hence the terminology "geometry-induced wave-function collapse." In particular, depending on the angular momentum and the energy of the particle, the inverse square-distance potential can generate bound states, conventional scattering states, and collapse states that are essentially an abnormal type of scattering states. The emergence of the collapse states was demonstrated through the LDOS that exhibits infinite oscillations with the energy near the zero energy point separating the scattering states from the bound states. We note that this feature of infinite oscillations was previously used to establish the atomic collapse states about a Coulomb impurity in graphene [7,32]. From a classical point of view, the geometry-induced and Coulomb-impurity induced collapse states share a common feature: the particle appears to fall into the center but will escape eventually either due to the finite ρ_0 or the complex eigenenergy. A key difference is that the geometry-induced collapse states uncovered here are a nonrelativistic quantum phenomenon while the atomic collapse states have a relativistic quantum origin.

The mechanism for the geometry-induced collapse states can be intuitively understood by noting that the sign of the effective radial potential is determined by [Eq. (10)]

$$\frac{l^2}{\alpha^2} - \frac{1-\alpha^2}{4\alpha^2},$$

where the second term is due to the mean curvature of the truncated cone. For the quantum states corresponding to zero angular momentum, the effective potential is attractive. The inverse squared distance dependence in Eq. (9) makes this type of geometry-induced "Coulomb impurity" much stronger than a usual Coulomb potential, thereby leading to collapse states with the classical picture of a particle falling into the center of the cone. For positive energy states, due to the reflection at ρ_0, the particle will eventually escape to infinity. More specifically, for $\alpha \to 1$, the geometry-induced attractive potential vanishes, and the quantum states degenerate to those described by the zeroth-order Bessel functions, which are scattering states in the 2D plane with a hard hole around the center. In this case, neither bound nor collapse states are possible. In the opposite extreme $\alpha \to 0$, the depth of the attractive potential becomes infinite, so only the bound states are possible. In between the two extreme cases where $0 < \alpha < 1$, collapse states can arise, which is promising to be observed in experiments.

ACKNOWLEDGMENTS

We thank Dr. H.-Y. Xu for discussions during the initial stage of this work. The work at Arizona State University was supported by AFOSR Grant No. FA9550-21-1-0186. The work at Lanzhou University was supported by National Natural Science Foundation of China under Grants No. 12175090 and No. 12047501.

APPENDIX A: GAUSSIAN AND MEAN CURVATURES OF A CONIC SURFACE

From the Gauss-Bonnet theorem

$$\iint_{\text{int}(\gamma)} K dA = 2\pi - \int_\gamma \kappa_g ds = 2\pi(1-\alpha), \tag{A1}$$

where the path γ is illustrated in Fig. 1, the Gaussian curvature satisfies the equation

$$\int_0^\infty K\alpha\rho d\rho \int_0^{2\pi} d\varphi = 2\pi(1-\alpha). \tag{A2}$$

The Gaussian curvature of a conic surface is thus given by

$$K = \left(\frac{1-\alpha}{\alpha}\right)\frac{\delta(\rho)}{\rho}, \tag{A3}$$

where the δ-function singularity originates from the apex of the cone. The mean curvature, the average of the maximal and minimal normal curvatures, is

$$K_M = \frac{\sqrt{1-\alpha^2}}{2\alpha\rho}, \tag{A4}$$

where $k_1 = 1/(\alpha\rho)$, $k_{1,n} = \sqrt{1-\alpha^2}/(\alpha\rho)$, and $k_2 = k_{2,n} = 0$.

APPENDIX B: SOLUTIONS OF THE SCHRÖDINGER EQUATION IN THE ANGULAR MOMENTUM REPRESENTATION

The general solution of Eq. (8) is

$$y(x) = AJ_\nu(x) + BY_\nu(x), \tag{B1}$$

where the orders ν and x are real or purely imaginary. The series representation of $J_\nu(x)$ is

$$J_\nu(x) = \sum_{k=0}^\infty \frac{(-1)^k}{k!\Gamma(k+\nu+1)}\left(\frac{x}{2}\right)^{2k+\nu}, \tag{B2}$$

which satisfies Eq. (8) regardless of whether the order and the argument are real or purely imaginary.

For clarity, the quantities ν and x are defined to be real. If ν is real, then $\nu \geqslant 0$; if ν is purely imaginary, then write ν as $i\nu$, $\nu > 0$. Similarly, if x is real, we have $x \geqslant 0$, and if x is purely imaginary we write x as ix, $x > 0$, respectively. Real ν values correspond to quantum states of nonzero angular momenta and purely imaginary ν values are associated with the zero angular momentum states. Real and purely imaginary x values are indicative of positive and negative energies, respectively. In particular, if the order ν or the argument x is purely imaginary, $J_\nu(x)$ and $Y_\nu(x)$ may not be real. Hence, it is necessary to give some extra definitions for the real Bessel functions [49,74].

If both ν and x are real, the real solution is

$$y(x) = AJ_\nu(x) + BY_\nu(x). \tag{B3}$$

If ν is real but ix is purely imaginary, the real solution is

$$y(x) = AI_\nu(x) + BK_\nu(x). \tag{B4}$$

For $i\nu$ purely imaginary and x real, the real solution is

$$y(x) = AF_{i\nu}(x) + BG_{i\nu}(x). \tag{B5}$$

If both $i\nu$ and ix are purely imaginary, the real solution is

$$y(x) = AL_{i\nu}(x) + BK_{i\nu}(x). \tag{B6}$$

All these solutions can be written as $J_\nu(x)$, $J_{-\nu}(x)$, $J_\nu(ix)$, $J_{-\nu}(ix)$, $J_{i\nu}(x)$, $J_{-i\nu}(x)$, $J_{i\nu}(ix)$, $J_{-i\nu}(ix)$, or their combinations:

$$I_\nu(x) = i^{-\nu}J_\nu(ix), \tag{B7}$$

$$K_\nu(x) = \pi[I_{-\nu}(x) - I_\nu(x)]/[2\sin(\nu\pi)], \tag{B8}$$

$$\begin{aligned} F_{i\nu}(x) &= \frac{1}{2}\left\{e^{-\pi\nu/2}H_{i\nu}^{(1)}(x) + e^{\pi\nu/2}H_{i\nu}^{(2)}(x)\right\} \\ &= \frac{1}{2}\{A_\nu J_{i\nu}(x) + iB_\nu Y_{i\nu}(x)\}, \end{aligned} \tag{B9}$$

$$\begin{aligned} G_{i\nu}(x) &= \frac{1}{2i}\left\{e^{-\pi\nu/2}H_{i\nu}^{(1)}(x) - e^{\pi\nu/2}H_{i\nu}^{(2)}(x)\right\} \\ &= \frac{1}{2i}\{B_\nu J_{i\nu}(x) + iA_\nu Y_{i\nu}(x)\}, \end{aligned} \tag{B10}$$

$$\begin{aligned} L_{i\nu}(x) &= iC_\nu\{I_{-i\nu}(x) + I_{i\nu}(x)\} \\ &= iC_\nu\left\{i^{i\nu}J_{-i\nu}(ix) + i^{-i\nu}J_{i\nu}(ix)\right\}, \end{aligned} \tag{B11}$$

$$\begin{aligned} K_{i\nu}(x) &= C_\nu\{I_{-i\nu}(x) - I_{i\nu}(x)\} \\ &= C_\nu\left\{i^{i\nu}J_{-i\nu}(ix) - i^{-i\nu}J_{i\nu}(ix)\right\}, \end{aligned} \tag{B12}$$

where

$$\begin{aligned} A_\nu &= e^{-\pi\nu/2} + e^{\pi\nu/2}, \\ B_\nu &= e^{-\pi\nu/2} - e^{\pi\nu/2}, \\ C_\nu &= \pi/[2\sin(i\nu\pi)]. \end{aligned}$$

The power series representations of $F_{i\nu}(x)$, $G_{i\nu}(x)$, $L_{i\nu}(x)$, and $K_{i\nu}(x)$ are given by [49]

$$F_{i\nu}(x) = D_\nu \sum_{s=0}^\infty \frac{(-1)^s\cos[\alpha_{\nu,s}(x)]}{\beta_{\nu,s}}\left(\frac{x}{2}\right)^{2s}, \tag{B13}$$

$$G_{i\nu}(x) = E_\nu \sum_{s=0}^\infty \frac{(-1)^s\sin[\alpha_{\nu,s}(x)]}{\beta_{\nu,s}}\left(\frac{x}{2}\right)^{2s}, \tag{B14}$$

$$L_{i\nu}(x) = M_\nu \sum_{s=0}^\infty \frac{\cos[\alpha_{\nu,s}(x)]}{\beta_{\nu,s}}\left(\frac{x}{2}\right)^{2s}, \tag{B15}$$

$$K_{i\nu}(x) = -M_\nu \sum_{s=0}^{\infty} \frac{\sin[\alpha_{\nu,s}(x)]}{\beta_{\nu,s}} \left(\frac{x}{2}\right)^{2s}, \tag{B16}$$

where

$$\alpha_{\nu,s}(x) = \nu \ln(x/2) - \phi_{\nu,s},$$
$$\beta_{\nu,s} = s![(\nu^2)(1^2+\nu^2)\cdots(s^2+\nu^2)]^{1/2},$$
$$D_\nu = \left(\frac{2\nu\tanh(\nu\pi/2)}{\pi}\right)^{1/2},$$
$$E_\nu = \left(\frac{2\nu\coth(\nu\pi/2)}{\pi}\right)^{1/2},$$
$$M_\nu = \left(\frac{\nu\pi}{\sinh(\nu\pi)}\right)^{1/2},$$

and $\phi_{\nu,s} = \arg\{\Gamma(1+s+i\nu)\}$, where $\phi_{\nu,s}$ is continuous for $0 < \nu < \infty$, with $\lim_{\nu\to 0}\phi_{\nu,s} = 0$.

For $x \to 0^+$, we have

$$F_{i\nu}(x) \to D_\nu \cos[\nu\ln(x/2) - \phi_{\nu,0}]/\nu, \tag{B17}$$

$$G_{i\nu}(x) \to E_\nu \sin[\nu\ln(x/2) - \phi_{\nu,0}]/\nu, \tag{B18}$$

$$L_{i\nu}(x) \to M_\nu \cos[\nu\ln(x/2) - \phi_{\nu,0}]/\nu, \tag{B19}$$

$$K_{i\nu}(x) \to -M_\nu \sin[\nu\ln(x/2) - \phi_{\nu,0}]/\nu. \tag{B20}$$

For $x \to +\infty$, we have

$$F_{i\nu}(x) \to J_0(x), \tag{B21}$$

$$G_{i\nu}(x) \to J_1(x), \tag{B22}$$

$$K_{i\nu}(x) \sim \left(\frac{\pi}{2x}\right)^{1/2} e^{-x}, \tag{B23}$$

$$L_{i\nu}(x) \sim \frac{1}{\sinh(\nu\pi)}\left(\frac{\pi}{2x}\right)^{1/2} e^{x}. \tag{B24}$$

For $\nu \to 0^+$ and any definitive x we have,

$$F_{i\nu}(x) \sim \lim_{\nu\to 0^+} \sum_{s=0}^{\infty} J_0(s,x)\cos(\phi_{\nu,s}) = J_0(x), \tag{B25}$$

$$\lim_{\nu\to 0^+} G_{i\nu}(x) \to Y_0(x) \tag{B26}$$

where

$$J_\nu(x) \equiv \sum_{s=0}^{\infty} J_\nu(s,x) = \sum_{s=0}^{\infty} \frac{(-1)^s}{s!\Gamma(s+\nu+1)}\left(\frac{x}{2}\right)^{2s+\nu}. \tag{B27}$$

For $x \to 0^+$ and $\nu \to 0^+$, the amplitudes of $F_{i\nu}$ and $G_{i\nu}$ tend to 1 and ∞, respectively. In this case, the function $G_{i\nu}$ can be neglected.

For $x \to +\infty$, we have

$$F_{i\nu}(x) \to \left(\frac{2}{\pi x}\right)^{1/2}\{\zeta(i\nu)\cos\alpha - \eta(i\nu)\sin\alpha\}, \tag{B28}$$

$$G_{i\nu}(x) \to \left(\frac{2}{\pi x}\right)^{1/2}\{\zeta(i\nu)\sin\alpha + \eta(i\nu)\cos\alpha\}, \tag{B29}$$

$$J_\nu(x) \to \left(\frac{2}{\pi x}\right)^{1/2}\cos\beta, \tag{B30}$$

where $\alpha \equiv x - \pi/4$ and $\beta = \alpha - \nu\pi/2$, and for $x \to +\infty$

$$\zeta(i\nu) \equiv \sum_{s=0}^{\infty}(-1)^s\frac{A_{2s}(i\nu)}{x^{2s}} \to 1$$
$$\eta(i\nu) \equiv \sum_{s=0}^{\infty}(-1)^s\frac{A_{2s+1}(i\nu)}{x^{2s+1}} \to 0,$$
$$A_s(i\nu) = \frac{(4(i\nu)^2 - 1^2)\cdots[-4(i\nu)^2 - (2s-1)^2]}{s!8^s},$$

which lead to Eqs. (B21) and (B22).

[1] H. Jensen and H. Koppe, Quantum mechanics with constraints, Ann. Phys. (NY) **63**, 586 (1971).

[2] R. C. T. da Costa, Quantum mechanics of a constrained particle, Phys. Rev. A **23**, 1982 (1981).

[3] A. Namiranian, M. Khajehpour, Y. A. Kolesnichenko, and S. Shevchenko, Conductivity of a two-dimensional curved microconstriction, Physica E **10**, 549 (2001).

[4] A. Szameit, F. Dreisow, M. Heinrich, R. Keil, S. Nolte, A. Tünnermann, and S. Longhi, Geometric Potential and Transport in Photonic Topological Crystals, Phys. Rev. Lett. **104**, 150403 (2010).

[5] J. Onoe, T. Ito, H. Shima, H. Yoshioka, and S.-I. Kimura, Observation of Riemannian geometric effects on electronic states, Europhys. Lett. **98**, 27001 (2012).

[6] G. H. Shortley, The inverse-cube central force field in quantum mechanics, Phys. Rev. **38**, 120 (1931).

[7] A. V. Shytov, M. I. Katsnelson, and L. S. Levitov, Atomic Collapse and Quasi–Rydberg States in Graphene, Phys. Rev. Lett. **99**, 246802 (2007).

[8] C. Filgueiras and F. Moraes, On the quantum dynamics of a point particle in conical space, Ann. Phys. (NY) **323**, 3150 (2008).

[9] A. Nicholson, Bound states and scattering in an r^2 potential, Aust. J. Phys. **15**, 174 (1962).

[10] L. D. Landau and E. M. Lifshitz, *Quantum Mechanics: Non-Relativistic Theory* (Pergamon, New York, 1981)

[11] S. A. Coon and B. R. Holstein, Anomalies in quantum mechanics: the 1/r 2 potential, Am. J. Phys. **70**, 513 (2002).

[12] H.-W. Hammer and B. G. Swingle, On the limit cycle for the 1/r2 potential in momentum space, Ann. Phys. (NY) **321**, 306 (2006).

[13] K. Case, Singular potentials, Phys. Rev. **80**, 797 (1950).

[14] Y. Nishida, Efimovian states of three charged particles, Phys. Rev. A **105**, L010802 (2022).
[15] V. Efimov, Energy levels arising from resonant two-body forces in a three-body system, Phys. Lett. B **33**, 563 (1970).
[16] V. Efimov, Energy levels of three resonantly interacting particles, Nucl. Phys. A **210**, 157 (1973).
[17] A. M. Perelomov and V. S. Popov, “Fall to the center” in quantum mechanics, Theor. Math. Phys. **4**, 664 (1970).
[18] S. Alliluev, The problem of collapse to the center in quantum mechanics, Sov. Phys. JETP **34**, 8 (1972).
[19] Y. Wang, D. Wong, A. V. Shytov, V. W. Brar, S. Choi, Q. Wu, H.-Z. Tsai, W. Regan, A. Zettl, R. K. Kawakami *et al.*, Observing atomic collapse resonances in artificial nuclei on graphene, Science **340**, 734 (2013).
[20] I. Pomeranchuk and Y. Smorodinsky, About the energy levels of systems with $z > 137$, J. Phys. USSR **9**, 97 (1945).
[21] Y. B. Zeldovich and V. S. Popov, Electronic structure of superheavy atoms, Sov. Phys. Usp. **14**, 673 (1972).
[22] W. Greiner, *Quantum Electrodynamics of Strong Fields* (Springer, New York, 1985).
[23] V. M. Pereira, A. H. Castro Neto, H. Y. Liang, and L. Mahadevan, Geometry, Mechanics, and Electronics of Singular Structures and Wrinkles in Graphene, Phys. Rev. Lett. **105**, 156603 (2010).
[24] C. Filgueiras, E. Silva, and F. Andrade, Nonrelativistic quantum dynamics on a cone with and without a constraining potential, J. Math. Phys. **53**, 122106 (2012).
[25] R. Salazar and G. Tellez, Constrained quantum mechanics: chaos in non-planar billiards, Eur. J. Phys. **33**, 965 (2012).
[26] L. Du, Y.-L. Wang, G.-H. Liang, G.-Z. Kang, X.-J. Liu, and H.-S. Zong, Curvature-induced bound states and coherent electron transport on the surface of a truncated cone, Physica E **76**, 28 (2016).
[27] Q.-D. Jiang and A. Balatsky, Geometric Induction in Chiral Superfluids, Phys. Rev. Lett. **129**, 016801 (2022).
[28] T. H. Boyer, Unfamiliar trajectories for a relativistic particle in a Kepler or Coulomb potential, Am. J. Phys. **72**, 992 (2004).
[29] A. V. Shytov, M. I. Katsnelson, and L. S. Levitov, Vacuum Polarization and Screening of Supercritical Impurities in Graphene, Phys. Rev. Lett. **99**, 236801 (2007).
[30] M. M. Fogler, D. S. Novikov, and B. I. Shklovskii, Screening of a hypercritical charge in graphene, Phys. Rev. B **76**, 233402 (2007).
[31] I. S. Terekhov, A. I. Milstein, V. N. Kotov, and O. P. Sushkov, Screening of Coulomb Impurities in Graphene, Phys. Rev. Lett. **100**, 076803 (2008).
[32] V. M. Pereira, J. Nilsson, and A. H. Castro Neto, Coulomb Impurity Problem in Graphene, Phys. Rev. Lett. **99**, 166802 (2007).
[33] A. C. Neto, V. N. Kotov, J. Nilsson, V. M. Pereira, N. M. Peres, and B. Uchoa, Adatoms in graphene, Solid State Commun. **149**, 1094 (2009).
[34] D. S. Novikov, Elastic scattering theory and transport in graphene, Phys. Rev. B **76**, 245435 (2007).
[35] V. N. Kotov, B. Uchoa, V. M. Pereira, F. Guinea, and A. H. Castro Neto, Electron-electron interactions in graphene: Current status and perspectives, Rev. Mod. Phys. **84**, 1067 (2012).
[36] Y. Wang, V. W. Brar, A. V. Shytov, Q. Wu, W. Regan, H.-Z. Tsai, A. Zettl, L. S. Levitov, and M. F. Crommie, Mapping Dirac quasiparticles near a single Coulomb impurity on graphene, Nat. Phys. **8**, 653 (2012).
[37] J. Mao, Y. Jiang, D. Moldovan, G. Li, K. Watanabe, T. Taniguchi, M. R. Masir, F. M. Peeters, and E. Y. Andrei, Realization of a tunable artificial atom at a supercritically charged vacancy in graphene, Nat. Phys. **12**, 545 (2016).
[38] Y. Jiang, J. Mao, D. Moldovan, M. R. Masir, G. Li, K. Watanabe, T. Taniguchi, F. M. Peeters, and E. Y. Andrei, Tuning a circular p-n junction in graphene from quantum confinement to optical guiding, Nat. Nanotechnol. **12**, 1045 (2017).
[39] O. Ovdat, J. Mao, Y. Jiang, E. Andrei, and E. Akkermans, Observing a scale anomaly and a universal quantum phase transition in graphene, Nat. Commun. **8**, 507 (2017).
[40] C.-D. Han, H.-Y. Xu, D. Huang, and Y.-C. Lai, Atomic collapse in pseudospin-1 systems, Phys. Rev. B **99**, 245413 (2019).
[41] C. W. J. Beenakker, Colloquium: Andreev reflection and Klein tunneling in graphene, Rev. Mod. Phys. **80**, 1337 (2008).
[42] B. S. DeWitt, Dynamical theory in curved spaces. I. A review of the classical and quantum action principles, Rev. Mod. Phys. **29**, 377 (1957).
[43] M. V. Entin and L. I. Magarill, Spin-orbit interaction of electrons on a curved surface, Phys. Rev. B **64**, 085330 (2001).
[44] J. Gravesen and M. Willatzen, Eigenstates of Möbius nanostructures including curvature effects, Phys. Rev. A **72**, 032108 (2005).
[45] E. Zhang, S. Zhang, and Q. Wang, Quantum transport in a curved one-dimensional quantum wire with spin-orbit interactions, Phys. Rev. B **75**, 085308 (2007).
[46] G. Ferrari and G. Cuoghi, Schrödinger Equation for a Particle on a Curved Surface in an Electric and Magnetic Field, Phys. Rev. Lett. **100**, 230403 (2008).
[47] H. Shima, H. Yoshioka, and J. Onoe, Geometry-driven shift in the Tomonaga-Luttinger exponent of deformed cylinders, Phys. Rev. B **79**, 201401(R) (2009).
[48] C. A. de Lima Ribeiro, C. Furtado, and F. Moraes, Bound states in the dynamics of a dipole in the presence of a conical defect, Mod. Phys. Lett. A **20**, 1991 (2005).
[49] T. Dunster, Bessel functions of purely imaginary order, with an application to second-order linear differential equations having a large parameter, SIAM J. Math. Anal. **21**, 995 (1990).
[50] J. Schwenk, S. Kim, J. Berwanger, F. Ghahari, D. Walkup, M. R. Slot, S. T. Le, W. G. Cullen, S. R. Blankenship, S. Vranjkovic *et al.*, Achieving μ ev tunneling resolution in an in-operando scanning tunneling microscopy, atomic force microscopy, and magnetotransport system for quantum materials research, Rev. Sci. Instrum. **91**, 071101 (2020).
[51] G. Binnig and H. Rohrer, Scanning tunneling microscopy - from birth to adolescence, Rev. Mod. Phys. **59**, 615 (1987).
[52] P. K. Hansma and J. Tersoff, Scanning tunneling microscopy, J. Appl. Phys. **61**, R1 (1987).
[53] J. Tersoff and D. R. Hamann, Theory of the scanning tunneling microscope, Phys. Rev. B **31**, 805 (1985).
[54] J. Li, W.-D. Schneider, and R. Berndt, Local density of states from spectroscopic scanning-tunneling-microscope images: Ag (111), Phys. Rev. B **56**, 7656 (1997).
[55] A. Krishnan, E. Dujardin, M. Treacy, J. Hugdahl, S. Lynum, and T. Ebbesen, Graphitic cones and the nucle-

ation of curved carbon surfaces, Nature (London) **388**, 451 (1997).

[56] H. Terrones, T. Hayashi, M. Munoz-Navia, M. Terrones, Y. Kim, N. Grobert, R. Kamalakaran, J. Dorantes-Davila, R. Escudero, M. Dresselhaus *et al.*, Graphitic cones in palladium catalysed carbon nanofibres, Chem. Phys. Lett. **343**, 241 (2001).

[57] S. Y. Zhou, G.-H. Gweon, A. V. Fedorov, P. N. First, W. A. de Heer, D.-H. Lee, F. Guinea, A. H. Castro Neto, and A. Lanzara, Substrate-induced bandgap opening in epitaxial graphene, Nat. Mater. **6**, 770 (2007).

[58] P. E. Lammert and V. H. Crespi, Topological Phases in Graphitic Cones, Phys. Rev. Lett. **85**, 5190 (2000).

[59] J. A. Jaszczak, G. W. Robinson, S. Dimovski, and Y. Gogotsi, Naturally occurring graphite cones, Carbon **41**, 2085 (2003).

[60] Y. Liu, X. Liu, Z. Ma, Y. He, and X. Zhang, A new preparation method of graphite cones from polycyclic aromatic hydrocarbons/polyimide composite carbon fibers, Carbon **196**, 128 (2022).

[61] M. Ge and K. Sattler, Observation of fullerene cones, Chem. Phys. Lett. **220**, 192 (1994).

[62] G. Zhang, X. Jiang, and E. Wang, Tubular graphite cones, Science **300**, 472 (2003).

[63] M. Berry, The geometric phase, Sci. Am. **259**, 46 (1988).

[64] J. Anandan, The geometric phase, Nature (London) **360**, 307 (1992).

[65] J. Anandan, J. Christian, and K. Wanelik, Resource letter GPP-1: Geometric phases in physics, Am. J. Phys. **65**, 180 (1997).

[66] E. Cohen, H. Larocque, F. Bouchard, F. Nejadsattari, Y. Gefen, and E. Karimi, Geometric phase from Aharonov-Bohm to Pancharatnam-Berry and beyond, Nat. Rev. Phys. **1**, 437 (2019).

[67] S. Azevedo and F. Moraes, Two-dimensional scattering by disclinations in monolayer graphite, J. Phys.: Condens. Matter **12**, 7421 (2000).

[68] J.-C. Charlier and G.-M. Rignanese, Electronic Structure of Carbon Nanocones, Phys. Rev. Lett. **86**, 5970 (2001).

[69] S. P. Jordan and V. H. Crespi, Theory of Carbon Nanocones: Mechanical Chiral Inversion of a Micron-Scale Three-Dimensional Object, Phys. Rev. Lett. **93**, 255504 (2004).

[70] P. E. Lammert and V. H. Crespi, Graphene cones: Classification by fictitious flux and electronic properties, Phys. Rev. B **69**, 035406 (2004).

[71] C. Furtado, F. Moraes, and A. d. M. Carvalho, Geometric phases in graphitic cones, Phys. Lett. A **372**, 5368 (2008).

[72] D. Akay, The effect of tilted magnetic field in graphene cone, Procedia Soc. Behav. Sci. **195**, 2913 (2015).

[73] R. Pincak, J. Smotlacha, and M. Pudlak, Calculation of the electronic structure near the tip of a graphitic nanocone, Physica B: Condens. Matter **441**, 58 (2014).

[74] F. Olver, *Asymptotics and Special Functions* (CRC, Boca Raton, FL, 1997).